An *In Vitro* Traumatic Injury Model to Examine the Response of Neurons to a Hydrodynamically-Induced Deformation

MICHELLE C. LAPLACA* and LAWRENCE E. THIBAULT†

*Department of Bioengineering, University of Pennsylvania, and the †Department of Neurosurgery, Division of Bioengineering, Allegheny University of the Health Sciences, Philadelphia, PA

Abstract—A novel *in vitro* system was developed to examine the effects of traumatic mechanical loading on individual cells. The cell shearing injury device (CSID) is a parallel disk viscometer that applies fluid shear stress with variable onset rate. The CSID was used in conjunction with microscopy and biochemical techniques to obtain a quantitative expression of the deformation and functional response of neurons to injury. Analytical and numerical approximations of the shear stress at the bottom disk were compared to determine the contribution of secondary flows. A significant portion of the shear stress was directed in the r-direction during start-up, and therefore the full Navier-Stokes equation was necessary to accurately describe the transient shear stress. When shear stress was applied at a high rate (800 dyne cm^{-2} sec^{-1}) to cultured neurons, a range of cell membrane strains (0.01 to 0.53) was obtained, suggesting inhomogeneity in cellular response. Functionally, cytosolic calcium and extracellular lactate dehydrogenase levels increased in response to high strain rate (>1 sec^{-1}) loading, compared with quasistatic (<1 sec^{-1}) loading. In addition, a subpopulation of the culture subjected to rapid deformation subsequently died. These strain rates are relevant to those shown to occur in traumatic injury, and, as such, the CSID is an appropriate model for studying the biomechanics and pathophysiology of neuronal injury.

Keywords—Cellular calcium, *In vitro* modeling, Mechanical loading, Shear stress, Strain rate.

INTRODUCTION

The high prevalence and socioeconomic impact of traumatic brain injury (TBI) has led to the development of numerous experimental models, from whole animal to cell preparations, to elucidate the cascade of events that lead to impaired function or tissue death. The integration of macroscopic and microscopic injury models is necessary to better understand the time course and the underlying mechanisms of TBI. Basic research can be incorporated with clinical data to determine tissue tolerance criteria and to advance pharmacological and rehabilitative therapies.

Inertial loading to the head, in particular, may cause serious impairment to the brain (11). Relevant loading conditions and the overall physiological response to traumatic inertial insults have been obtained and extensively studied in whole animal preparations (10). These loading parameters were subsequently applied to physical models of the brain (18) to obtain spatial and temporal patterns of deformation associated with TBI. These deformation patterns, in turn, have been used as the input to isolated neural tissues and cells (2,7,23). Typical strains and strain rates in tissues during inertial loading that produce injury are 0.1 to 0.3 and 1 to 10 sec^{-1}, respectively (29).

TBI is initiated when the level of an insult surpasses the structural integrity of the brain or its substructures and subsequently triggers many interdependent chemical events (9,27). Ultimately, the cellular and molecular mechanisms that precipitate the systemic response and the associated time course must be deciphered to intervene effectively. Understanding the response of a single cell to mechanical injury is an important step in the development of efficacious treatments and improved injury tolerance criteria. The numerous molecular mechanisms of cellular defense are complex and interrelated; they are virtually impossible to identify in a whole organism. The isolation of cells from a whole organism presents a simple system for which input parameters can be controlled to characterize cellular response to traumatic loading. In addition, well-characterized cellular injury models provide an opportunity for testing potential drug therapies in an experimental setting, a necessary step before introduction of such agents to whole animal or clinical paradigms.

A number of cell culture models have been developed to investigate the events following a mechanical insult. For example, Winston *et al.* (32) developed a flexible substrate system that was further modified by Cargill and Thibault (2) to apply a vacuum pulse to injure neural-like cells while monitoring intracellular free calcium concentration

$([Ca^{2+}]_i)$. Recently, Ellis et al. (5) used a similar system to stretch astrocytes rapidly and examined cellular morphology and membrane integrity. While these systems stretch adherent cells at varying rates, the actual strain on the cells is unknown and must be approximated as that of the deformed substrate. In addition, because the cells are not in focus during substrate deformation, it is difficult to acquire immediate functional data, especially for quasistatic insults. An acceleration injury was also modeled by the multiple impact device of Lucas and Wolf (17), although the acute cellular deformation was unknown. Shepard et al. (26) designed a barotrauma chamber to model traumatic injury to glial cells and assessed injury by trypan blue staining. Even though cells may undergo pressure changes during an acceleration injury, the level of stretch in this model is also unknown.

A biomechanical approach to modeling traumatic injury in vitro begins by selecting forces or deformations, and their respective rates, which mimic a specific injury (Fig. 1). Because the mechanical and functional responses of a cell are dependent on the parameters of the initial mechanical insult, the loading conditions must be reproducible over a relevant range of magnitudes and rates. Quasistatic controls must be attainable when modeling inertially induced injury to determine the rate dependence of the cellular response. The cell shearing injury device (CSID) was designed to deliver a variable controlled fluid shear stress as the mechanical input to deform neurons at rates associated with both quasistatic loading (<1 sec^{-1}) and inertial injury (>1 sec^{-1}). Once the loading conditions required to produce relevant cell strains and strain rates
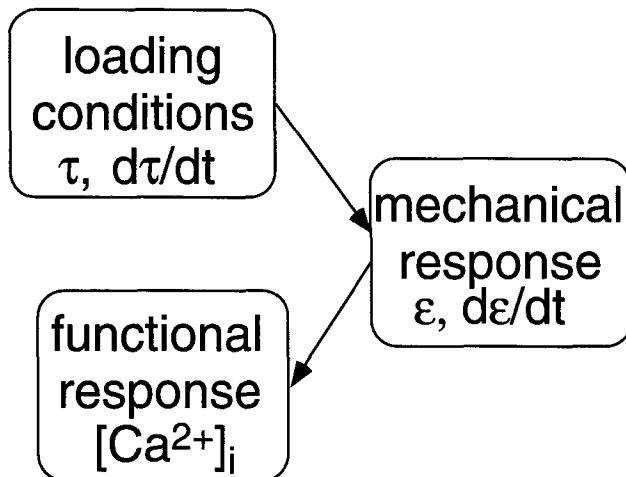

FIGURE 1. The biomechanical approach to modeling traumatic injury in vitro. A set of loading conditions are selected to mimic best the injury to be modeled and to elicit the appropriate mechanical response. Variable rates of fluid shear stress, $d\tau/dt$, are used here to deform neurons (ϵ = strain, $d\epsilon/dt$ = strain rate) in a noncontact fashion. Then, functional responses, such as intracellular free calcium measurements ($[Ca^{2+}]_i$), can be analyzed and correlated to loading conditions.

were determined, these conditions were applied while a functional response, namely $[Ca^{2+}]_i$, was monitored. Examining the effects of controlled mechanical loading on cultured neural cells will provide valuable information in understanding cellular injury mechanisms.

The fluid shear stress input to the cells in the CSID was produced by rotating a top disk that transferred momentum through a fluid-filled chamber to a stationary disk on the bottom of the chamber where the cells were cultured. Many similar configurations have been previously used to apply physiological levels of shear stress to cultured cells in both steady and pulsatile flows (3,4,19). A parallel disk design was chosen over a cone disk configuration to produce a shear stress gradient rather than a constant shear stress over the plate, yielding more information about insult magnitude per experiment. An advantage of the CSID over similar shearing devices is that rapid loading rates may be applied ($\sim$800 dyne cm^{-2} sec^{-1}), permitting analysis of rate dependence. In addition, a clear light path permits direct visualization of the cells in either incandescent or fluorescent light microscope configurations.

Externally applied stresses on adherent cells in culture can produce changes in adhesion dynamics, total cell deformation, and rearrangement of cytoskeletal and membrane constituents, such as surface proteins, receptors, and phospholipid molecules, all of which depend on the material properties of the particular cell and influence the total physiological response, such as intracellular signaling (31). In particular, changes in membrane properties, such as permeability, may lead to the unwanted influx of extracellular milieu and efflux of cytosolic components. The membrane deformation and deformation rate, therefore, are of specific interest when modeling an inertial insult for the purpose of assessing functional outcome. Because the gross deformations and deformation rates associated with inertial loading are known, these provide an estimate of the loading to individual components. The deformation, or strain, and the corresponding rate, therefore, constitute the mechanical response to the imposed loading conditions.

Local cell strain has been extensively studied in single suspended cells using micropipette aspiration (22) to determine mechanical properties (6,24). Confocal microscopy in combination with geometric modeling has been used to estimate cellular deformation in chondrocytes subjected to a mechanical stress (12). Cytoplasmic strains and strain rates in locomoting neutrophils have been examined by following groups of phagocytized microbeads over time (28). A similar technique was used to calculate the strain fields on the surface of adherent cells (1,14) and was employed in the present study.

Measurement of $[Ca^{2+}]_i$ was also obtained in real-time, permitting functional changes to be related to mechanical strain and strain rate, a crucial step in understanding the sequelae of traumatic injury. Although intracellular free

calcium is vital for many cell regulatory and signaling processes, an excessive sustained accumulation is toxic and believed to mediate cellular injury and death (20,25,30). Disturbances of membrane integrity, membrane potential, and transport processes may cause an influx of calcium ions and lead to cellular damage.

The magnitude and rate of strain are determining factors in the cell's ability to maintain ion homeostasis (29). It was hypothesized that mammalian cells have a critical threshold of strain and strain rate, above which they succumb and fail both structurally and functionally. Thus, under high rate loading conditions (>1 sec^{-1}), tissue deformation causes initial membrane damage, allowing non-specific ionic shifts across the membrane, leading to mass depolarization and a deleterious influx of free calcium ions.

In the present study, we have characterized the fluid shear stress produced by the CSID through analytical, numerical, and experimental means. We have shown that it is capable of deforming cultured neurons at rates high enough to incur functional compromise.

DESCRIPTION OF CSID

The device chosen to stimulate the cultured cells mechanically was a parallel disk viscometer (Fig. 2). The boundary layer formed on a free rotating disk under similar conditions (thickness $\delta = 3.6\sqrt{v/\omega}$) (16) is on the same order of magnitude as the gap distance; therefore, it was valid to approximate the flow field as Couette flow. The characteristic Reynolds number (Re $= h^2\omega/v$) for operating conditions ranged between 1 and 25. The cell substrate was a flat quartz disk held by vacuum in a stationary cell plate on the microscope stage. A cylinder with a flat quartz bottom comprised the top disk and was driven by a low inertia direct current motor (Pacific Scientific, Rockford, IL, USA) coupled through a timing belt. Radial and axial thrusts in the load (rotating cylinder) were taken up by two opposing angular contact ball bearings.

The gap distance, h, between the two quartz disks was adjusted by means of a vertical micrometer attached to the cylinder, which was set before each experiment. The gap distance was calibrated by adding known volumes of water to the chamber and adjusting the micrometer until the fluid completely touched the top cylinder and the edges of the chamber. Because the shear stress varies radially, the radial position of the cells was found using x- and y-coordinate vernier rulers. The cell plate also has injection and ejection ports to aid in the perfusion of buffers, agonists, or antagonists during experimentation. All experiments were performed at 37 ± 0.5°C using a custom-built heating control system (Dowty Electronic Co., Brandon, VT, USA) with a nickel/chromium heating element electrically insulated with fiberglass sleeving, and a thermo-
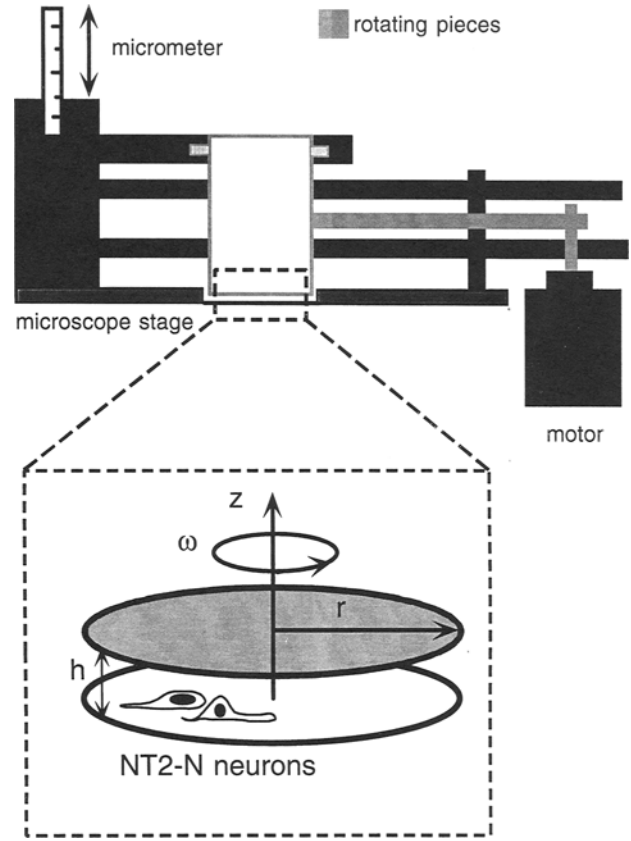

FIGURE 2. The CSID with designated directional components. Cells are on a stationary coverslip in a chamber filled with buffer. Shear stress at the cell plate is generated by angular velocity of the top cylinder, which is coupled to a motor. The cylindrical variables used in analyses are illustrated: where h is gap distance in the z-direction, ω is angular speed in the θ-direction, and r is radial distance in the r-direction.

couple feedback (Omega Engineering, Stamford, CT, USA).

Output voltage to the motor and back electromagnetic force (EMF) feedback was controlled by an interface board (Automation for Industry, Inc., Littleton, MA, USA). Maximum acceleration of the motor was 10,500 rad/sec^2, and the motor accelerated the load in 4.15 msec. This takes into account a reduction in speed compromised for an increase in torque by using a 4:1 gear ratio. The motor speed varied linearly with input voltage ($r^2 = 0.99$).

METHODS

Analytical Solution

The velocity patterns in the chamber are dictated by the Navier-Stokes equation:

$$\rho\left(\frac{\partial \mathbf{v}}{\partial t} + \mathbf{v} \cdot \nabla \mathbf{v}\right) = -\nabla p + \rho \mathbf{g} + \mu \nabla^2 \mathbf{v}. \tag{1}$$

(The directional components are illustrated in Fig. 2.) The fluid was treated as Newtonian, and the flow as incompressible and symmetric in the θ-direction. In the θ-direction, the Navier-Stokes equation reduces to the following partial differential equation:

$$\frac{\partial v_\theta}{\partial t} + v_r \frac{\partial v_\theta}{\partial r} + \frac{v_r v_\theta}{r} + v_z \frac{\partial v_\theta}{\partial z} = v \left[\frac{\partial^2 v_\theta}{\partial r^2} + \frac{1}{r} \frac{\partial v_\theta}{\partial r} - \frac{v_\theta}{r^2} + \frac{\partial^2 v_\theta}{\partial z^2} \right],$$
(2)

for which no closed-form solution exists.

A first-order approximation of the azimuthal velocity upon start-up was obtained by setting v_r and v_z equal to 0. This simplifying assumption was assumed to be valid because the radius is much greater than the gap distance ($r/h \gg 50$), and thus the geometry can be approximated as two infinite flat parallel disks. Simplifying Eq. 2 and substituting nondimensional terms ($r^* = r/h$; $t^* = tv/h^2$; $z^* = z/h$; $v_\theta = v_\theta/h\omega$) yields:

$$\frac{\partial v_\theta^*}{\partial t^*} = \left[\frac{\partial^2 v_\theta^*}{\partial r^{*2}} + \frac{1}{r^*} \frac{\partial v_\theta^*}{\partial r^*} - \frac{v_\theta^*}{r^{*2}} + \frac{\partial^2 v_\theta^*}{\partial z^{*2}} \right].$$
(3)

In start-up problems, it is convenient to solve for the difference between the steady-state solution and the actual velocity (15):

$$v^*_\theta = v_\theta^* - v_{ss}^* = v_\theta^* - r^* z^*; \ (v_{ss} = \frac{r\omega z}{h}).$$
(4)

Assuming the solution has the form $v_\theta' = rG(z)H(t)$, the equation further reduces to a parabolic partial differential equation:

$$\frac{\partial v'_\theta{}^*}{\partial t^*} = \left[\frac{\partial^2 v'_\theta{}^*}{\partial z^{*2}} \right].$$
(5)

The boundary conditions are:

$v'_\theta{}^*(r^*,0,t^*) = 0 \quad \text{all} \quad t^* \geq 0$

$v'_\theta{}^*(r^*1,t^*) = -r^* z^* \quad \text{all} \quad t^* \geq 0.$
(6a)

The initial condition is:

$$v'_\theta{}^*(r^*,z^*,0) = 0.$$
(6b)

Solving by the method of separation of variables, the azimuthal velocity component is:

$v_\theta{}^*(r^*,z^*,t^*) =$

$$r^* z^* + 2r^* \sum_{n=1}^{\infty} \frac{(-1)^n}{n\pi} \exp(-n^2\pi^2 t^*)\sin(n\pi z^*).$$
(7)

For a Newtonian fluid, the shear stress acting on the wall is the velocity gradient multiplied by the viscosity. The shear stress at the cell plate can then be approximated by the following expression (in dimensional terms):

$\tau_{\text{cell plate}} =$

$$-\mu(\frac{\partial v_\theta}{\partial z})_{z=0} = -\mu \frac{\omega r}{h} \left[1 + 2 \sum_{n=1}^{\infty} (-1)^n \exp(\frac{-n^2\pi^2 vt}{h^2}) \right].$$
(8a)

The steady-state solution is approximated by:

$$\tau_{\text{cell plate}} = \lim_{t \to \infty} (-\mu(\frac{\partial v_\theta}{\partial z})_{z=0})_{t \to \infty} = -\mu \frac{\omega r}{h}.$$
(8b)

Flow Visualization

To visualize the flow patterns during start-up, food coloring (0.5 μl) was added to a glass-bottomed replica of the cell plate 0.5 cm from the outer edge and allowed to dry. Distilled water was added slowly and the top cylinder lowered and the gap distance set to either 0.025 or 0.050 cm. The top cylinder was started impulsively to final speeds of 500 or 1000 rpm (52.5 and 105 rad/s). For steady-state runs, the dye was injected from a port in the outer edge of the bottom plate after the top cylinder was accelerated. Video was recorded (Panasonic SVHS AG-1960) and superimposed with a frame code generator (Sony FCG-700). Video was slowed down to one frame per second to survey the frames of the first few revolutions after dye dissolution.

Numerical Solution

The full Navier-Stokes equation (Eq. 1) was solved by the finite element method using the numerical analysis program FIDAP (F.D.I., Evanston, IL, USA) on a IBM RS-6000 computer (IBM Corp., Armonk, NY, USA) to determine the contribution of the radial velocity component to the shear stress at the bottom disk. An axisymmetric model representing the flow domain was constructed using 9-nodal quadrilateral elements. The meshing strategy was optimized to produce finer meshing in the regions of higher flow gradient near the outer radius. Numerical simulations were conducted for gap distances of 0.025 and 0.050 cm and top disk speeds of 52.5 and 105 rad/s. For all simulations, the no-slip condition was applied at both disk surfaces and chamber sides. For the transient analysis, the acceleration of the top plate was prescribed as measured experimentally from the back EMF of the motor (Figure 3). The method of successive substitutions with residual vector convergence tolerance of 2% was used to obtain steady-state solutions, whereas an optimized implicit trapezoidal integrator with variable time steps was used for the transient analyses.

Cell Culture

NTera 2/cl.D1 (NT2) cells were maintained according to the methods outlined by Pleasure et al. (21). Briefly, undifferentiated NT2 cells were differentiated by treating with 10 μM retinoic acid (Sigma Chemical Co., St. Louis,
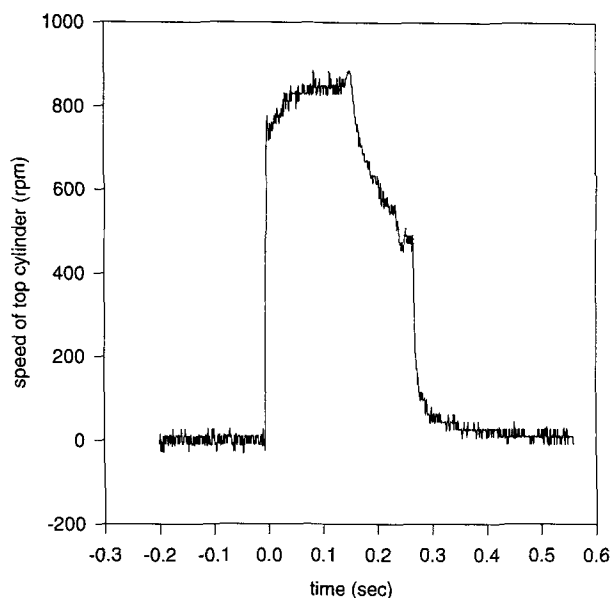
FIGURE 3. The time *versus* velocity profile of the motor used with the CSID as measured by the back EMF signal. Signal shown is a sample pulse for a rapid acceleration, or high rate, insult. Angular velocity is given in revolutions per minute (rpm).

MO, USA) in Dulbecco's modified Eagle's medium (Gibco BRL, Grand Island, NY, USA)/10% fetal bovine serum (HyClone, Logan, UT, USA) with pen/strep (Gibco BRL) twice a week for 5 weeks. Differentiated neurons (NT2-N cells), maintained in Dulbecco's modified Eagle's medium/5% fetal bovine serum with mitotic inhibitors and pen/strep, were seeded onto poly-D-lysine (10 μg/ml) and Matrigel (Collaborative Biomedical Research Products, Bedford, MA, USA) coated disks at a surface density of $1.2 \times 10^5/cm^2$, and no differences in cell density were observed across the disk in the 21 days before experimentation.

Measurement of Cell Strain

A 1:100 dispersion Fluoresbrite 0.5-μm diameter microspheres (3.64×10^{11}/ml) (Polysciences, Inc., Warrington, PA, USA) in control saline solution [CSS (in mM): 120 NaCl, 5.4 KCl, 0.8 $MgCl_2$, 1.8 $CaCl_2$, 25 HEPES, 15 glucose] was allowed to attach (10 min at 37°/5% CO_2) to the plasma membrane before stimulus. The cells were placed in the CSID as described below, and video was recorded (Panasonic SVHS AG-1960) and superimposed with a frame code generator (Sony FCG-700) before, during, and after the mechanical stimulus. The video was slowed down to one frame per second, and selected frames were chosen and downloaded to a Macintosh computer for analysis using NIH Image 1.54. The second frame (66 msec) after loading was used to measure strains during the stimulus to minimize out-of-focus error associated with

motor start-up. Beads were digitized, and the Lagrangian strains were computed by tracking triads of beads in the $r\theta$-plane (Fig. 4). A computer program to locate the intensity center of a microsphere was used to minimize error associated with manual measurement. Principal strains were therefore calculated to within ± 2% of the total principal strains, which is far less variability than seen among a population of cells.

The principal axes were defined as the r- and θ-directions to correspond with the geometry of the system and verified by solving the eigenvalue Eq. 12 below. For plane strain:

$$dS^2 - dS_o^2 = 2E_{ij}da_i da_j \text{ where } i, j = 1 \text{ to } 2 \ (1, 2 = r, \theta),$$
$$(9)$$

and E_{ij} is the Lagrangian strain tensor given by:

$$E_{ij} = \frac{1}{2}(\frac{\partial u_i}{\partial a_j} + \frac{\partial u_j}{\partial a_i} + \frac{\partial u_k}{\partial a_i}\frac{\partial u_k}{\partial a_j}). \qquad (10)$$

Equation 9 was expanded to find the finite plane strain components E_{11}, E_{12}, and E_{22}:
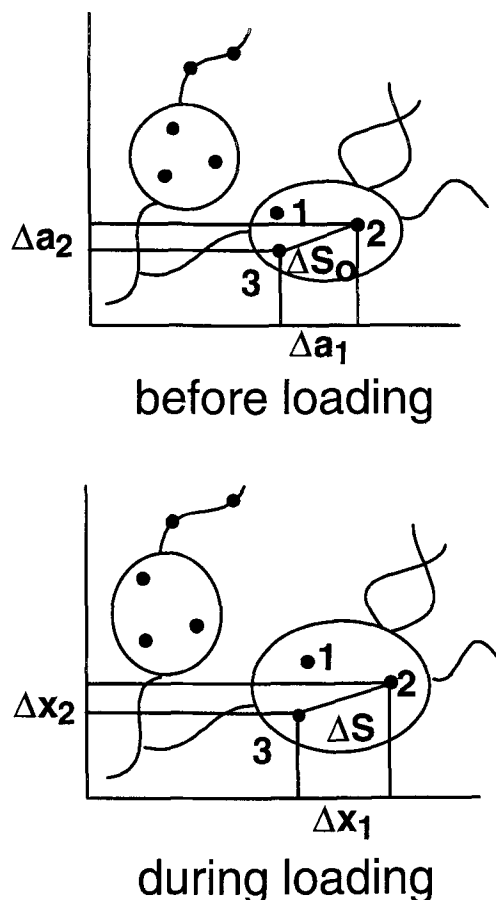

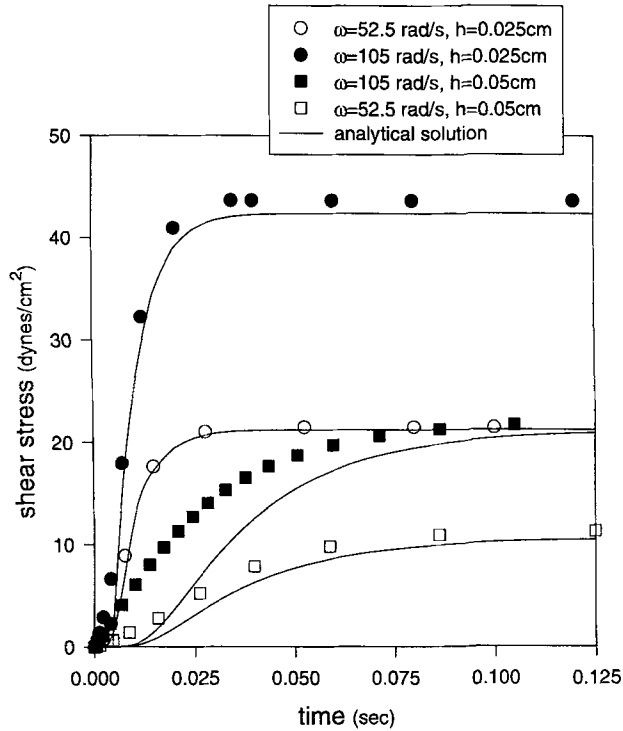FIGURE 4. The triad method used to calculate cellular strain.

FIGURE 5. Analytical and numerical solutions to shear stress at the bottom disk in the CSID. Symbols represent results from FIDAP simulations for each case of angular speed, ω, and gap distance, h, denoted. Lines are the corresponding results from analytical approximations.

$$(\Delta S^2 - \Delta S_o^2)_i = 2(E_{11}\Delta a_1 \Delta a_1 + 2E_{12}\Delta a_1 \Delta a_2 + E_{22}\Delta a_2 \Delta a_2)_i, \quad i = 1 \text{ to } 3. \quad (11)$$

The principal strains and directions were found by solving the eigenvalue problem:

$$(E_{ij} - E_k \delta_{ij})v_i^{(k)} = 0 \quad \text{for} \quad k = 1, 2. \quad (12)$$

E_1 was taken to be the larger of the two principal strains and is the strain reported in the results. A similar method was used to calculate the cytoplasmic deformation in locomoting neutrophils (28).

$[Ca^{2+}]_i$ Measurement

$[Ca^{2+}]_i$ was measured using the dual excitation calcium-sensitive dye Fura-2 (Molecular Probes, Eugene, OR, USA) and a quantitative fluorimeter (Olympus and Hamamatsu, Japan). Cells were rinsed with CSS and loaded by a 30-min incubation at 25°C with 3.6 μM of the acetoxymethyl ester of Fura-2 (Fura-2 AM). The cells were then rinsed with CSS and mounted on an Olympus IMT-2 inverted microscope (Olympus, Japan). The injury device was lowered onto the cells as described below. Fura-2 was excited at 340 and 360 nm to detect changes in $[Ca^{2+}]_i$, which cause the ratio of the emission spectra at these wavelengths to change. Background fluorescence was subtracted before $[Ca^{2+}]_i$ determination. A calibration

curve was generated (Molecular Probes) and used to calculate the $[Ca^{2+}]_i$ from individual cells in conjunction with the fluorescence imaging software CASALS (v.2.2E; Olympus, Japan).

Simultaneous strain and calcium measurements were done by first incubating cells with Fura-2 AM for 25 min. After a buffer rinse, a 1:100 solution of carboxyl-coated blue FluoSpheres (2.91 $\times$ 10^{11}/ml, 0.5 μm diameter, excitation wavelength: 360 nm, emission wavelength: 415 nm) (Molecular Probes) was added to the cells and incubated for 10 min at 37°C/5% CO_2. Cells were rinsed and experiments were conducted on a Nikon Diaphot microscope coupled to a silicon-intensified tube camera (Hamamatsu, Japan) that recorded directly to an optical memory disk recorder (Panasonic, Japan) at 30 frames per second. A baseline image at 360 nm was taken, and then experiments were performed during 340 nm excitation. A 360 nm image was taken at the end and averaged with the first prior to ratio analysis. Both beads and Fura dye were visible at the emission of these wavelengths. No more than 100 frames were collected to minimize photobleaching, and measurements were taken from the second frame after the start of the stimulus. Strain measurements were done in MetaMorph (Universal Imaging Corporation, West Chester, PA, USA), and calcium ratios were analyzed using MetaFluor (Universal Imaging Corporation).

Injury Paradigm

The same protocol was used for both deformation and $[Ca^{2+}]_i$ experiments under injury and control conditions. Cells were prepared either to study deformation (microbead incubation), $[Ca^{2+}]_i$ (Fura 2-AM incubation), or both. The quartz disk was then placed in the microscope stage cell plate and held in place using a vacuum. CSS was added to the cells, and the top cylinder was lowered onto the microscope stage and adjusted using the vertical micrometer to a gap distance of 0.025 cm. The motor controlling the rotation of the top cylinder was either triggered from the motor control interface board (rise time = 25 msec, duration = 200 msec, high strain rate protocol) or by manually dialing the potentiometer controlling the current to the motor (rise time = 2.0 sec, duration = 4.0 sec, low strain rate protocol).

Injury Assessment

Lactate dehydrogenase (LDH) release was assayed from the extracellular bath (Sigma) before the mechanical stimulus, immediately after the stimulus, and at 30 min, 3 hr, 15 hr, and 24 hr poststimulus to measure any loss in membrane integrity. Cell viability in individual cells was assessed using calcein (4 μM) and ethidium homodimer-1 (4 μM) fluorescent probes (Live/Dead Viability/ Cytotoxicity kit; Molecular Probes) at 24 hr for different
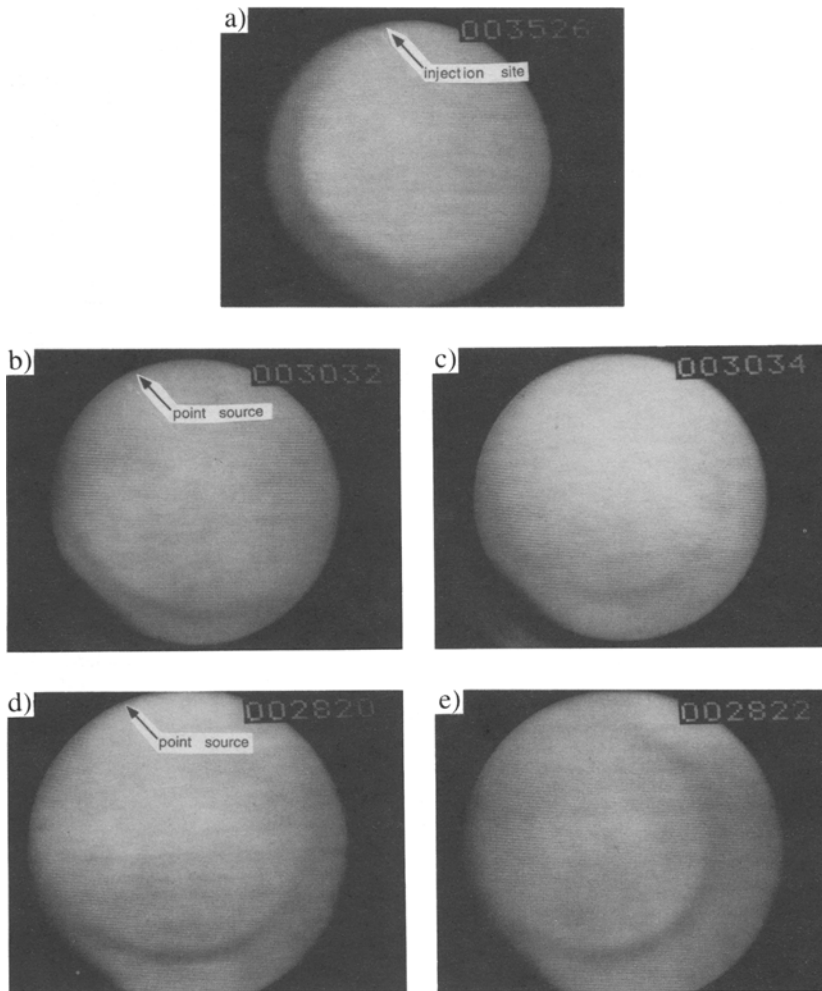
FIGURE 6. Flow visualization in the CSID. (a) Steady state, $h = 0.025$ cm; (b) start-up $t = 0$, $h = 0.025$ cm; (c) start-up $t = 66$ msec, $h = 0.025$ cm; (d) start-up $t = 0$, $h = 0.050$ cm; (e) start-up $t = 66$ msec; (f) components of the velocity shown for two separate dye experiments. The v_r component is smaller during steady state and start-up for narrow ($h/r < 0.01$) gap distances, depicted in the outer trace, than for larger ($h/r > 0.01$) gap distances, as illustrated in the inner trace.
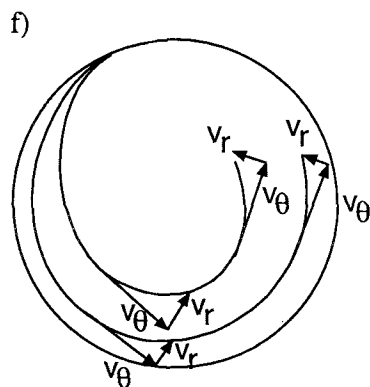
radial distances because LDH measurements represent an average value for the entire culture dish.

RESULTS

The analytical approximation to the start-up problem is plotted in Fig. 5 and shows the development of the shear stress at the bottom disk for different speeds and gap distances at a fixed radius (1.0 cm). Although the exponential terms decay with n^2, the first 10 terms of the series expansion contributed to the momentum diffusion from the rotating disk to the cells for early time points (<20 msec). Whereas the steady shear stress magnitude can be controlled by both the speed of the rotating disk and the gap

TABLE 1. Comparison of analytical and numerical calculations for shear stress values and times to develop maximum stress at the bottom disk of the CSID for a fixed radius ($r = 1.0$ cm).

Analytical/ Numerical	$h = 0.025$ cm $\omega = 52.5$ rad/sec	$h = 0.025$ cm $\omega = 105$ rad/sec	$h = 0.05$ cm $\omega = 52.5$ rad/sec	$h = 0.05$ cm $\omega = 105$ rad/sec
Steady analysis τ_{max} (dyne/cm^2)	21.21/21.46	42.42/43.89	10.60/11.35	21.21/22.06
Unsteady analysis τ_{max} (dyne/cm^2)	21.21/21.45	42.42/43.64	10.60/11.35	21.21/22.06
Time to reach 95% (msec)	23.8/25.2	23.8/24.4	93.5/83.7	93.5/79.6

distance between disks, the transient profile is dictated by the gap distance. The shear stress was calculated to develop to 95% in 23.8 msec for the small gap distance, 0.025 cm, for both 52.5 and 105 rad/sec. For a 0.050 cm gap distance, shear stress at the bottom disk took 93.5 msec to develop to 95% for both angular velocities.

Flow visualization indicated that the flow was laminar and undisturbed for gap distances of 0.025 and 0.050 cm. At a gap distance of 0.100 cm, recirculation patterns in the outer radial half of the chamber were evident in the first revolution, probably due to boundary layer separation; therefore, this setting was not used. When viewed from the z-axis, a spiraling pattern of the dye toward the center of the disk suggested the presence of secondary flow due to inertial effects (Fig. 6). Flow in the radial direction contributed to the velocity field for both start-up and steady state profiles. The ratio of v_r to v_θ was less for steady-state flow than for the start-up regime and less for smaller gap distances, which better approximate infinite disks.

Steady-state shear stress at the bottom of the chamber was slightly higher when obtained from numerical solutions schemes (within 7%) (Table 1). Velocity in the z-direction was negligible for all cases. The time course for shear stress development in the unsteady problem for the numerical computation agreed reasonably well with the analytical approximation. Simulations for a gap distance of 0.025 cm and both angular velocities tested (52.5 and 105 rad/sec) reached 95% of steady state at 25.2 and 24.7 msec, which were slightly longer times (within 6%) than analytical calculations. The larger gap distance cases, on the other hand, developed to 95% of the steady state in less time, 83.7 msec and 79.6 msec (within 15%).

τ_{zr} dominated the total shear stress the first 50 msec for the larger gap distance and the first 8 msec for the smaller
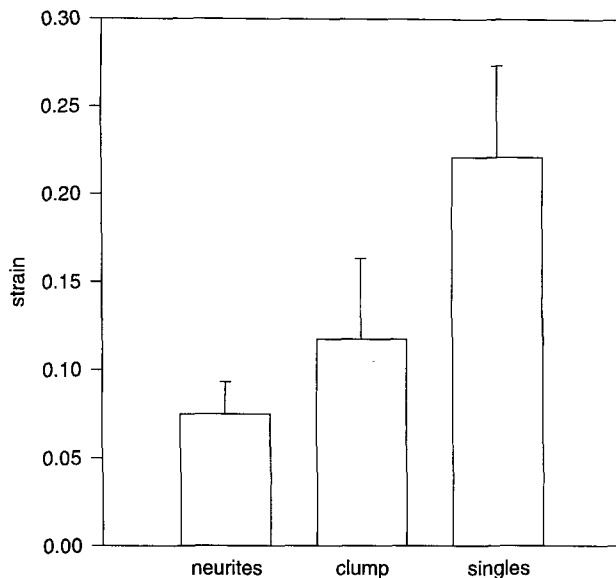

FIGURE 7. Comparison of strain in cell processes, or neurites, cells within a clump, and individual neurons. Bars represent the average strain for 8 neurites, 13 cells within cell aggregates, and 19 single cells. Error bars are the standard error of the means.
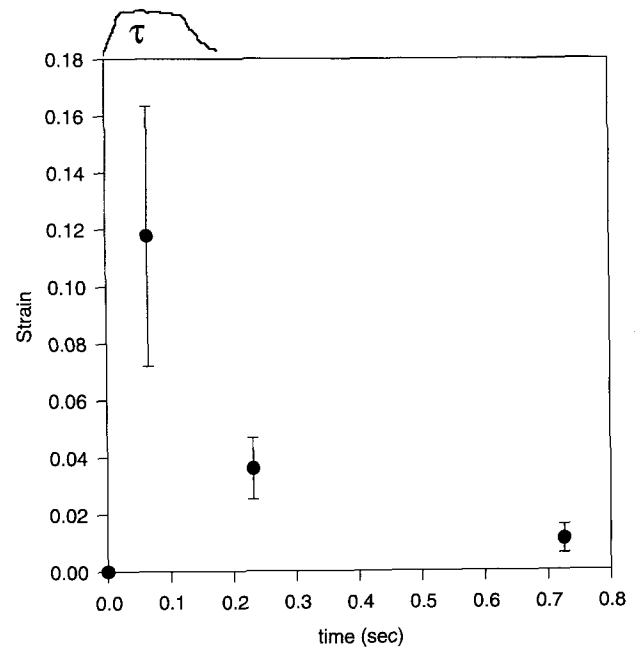

FIGURE 8. Time course of strain in neurons in the same aggregate or clump of cells. The same eight cells are averaged for each time point. Error bars represent the standard error of the means. The fluid shear stress, τ, illustrated above the graph, corresponds to the following loading parameters: magnitude, 20 dyne/cm^2; rise time, 25 msec; and duration, 200 msec.
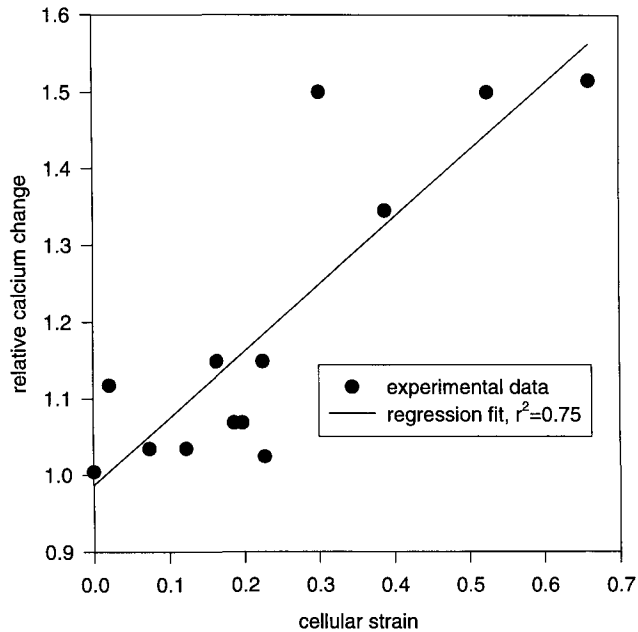
FIGURE 9. The correlation between cellular strain and relative calcium changes. A value of 1.0 corresponds to no change. $n = 14$ cells for 8 separate experiments.

gap distance. For example, at steady-state conditions τ_{zr} was 67% of the total stress for the larger gap distance *versus* 31% for the smaller gap distance, and $\tau_{z\theta}$ was 74% *versus* 95%, respectively. This shifting of dominant flow patterns indicated the better approximation of infinite disks (where τ_{zr} equals 0) for smaller gap distances.

The strain and strain rate for cell bodies and processes of the NT2-N cells were found to vary widely for a given shear stress stimulus and arrangement (Fig. 7). All strains reported are the larger principal strains, in the principal direction, usually in the θ-direction, whereas the smaller principal strains were almost always very close to 0. For an insult with a magnitude of 20 dyne/cm^2, a rise time of 25 msec, and a duration of 200 msec, strains varied from 0.01 to 0.52 (0.18 ± 0.03, mean ± SEM, $n = 32$ cell bodies). Cells in clumps of four or more had lower average strains (0.12 ± 0.05, mean ± SEM, $n = 13$ cell bodies) than single neurons (0.22 ± 0.05, mean ± SEM, $n = 19$ cell bodies). Uniaxial strains in the neurites, calculated as a stretch ratio [$\lambda = (l - l_o)/l_o$] were also measured and found to vary from 0.02 to 0.17 (0.08 ± 0.02, means ± SEM, $n = 8$ neurites).

The strain from the cells within a group of eight cells over several frames was calculated to obtain a transient response to loading (Fig. 8). At the onset of loading, these strains corresponded to strain rates >1 sec^{-1}, a rate thought to be a threshold for cellular and tissue dysfunctions. Because the temporal resolution of standard video frame sampling is 30 Hz, typical strain rates used were estimated to be 2 to 10 sec^{-1} (high strain rate) and 0.02 to 0.1 sec^{-1}

(low strain rate). The rise time of the shear stress was either 2 sec or 25 msec, depending on the loading protocol, and this was taken into consideration when approximating strain rates. Directly after the stress was removed, strain levels dropped to 0.04 ± 0.01 (mean ± SEM, $n = 8$ cells) from 0.12 ± 0.05. By 0.5 sec after the stress was removed, most of the cells had returned to the preloaded deformation state (0.01 ± 0.005), indicating that the beads were firmly attached to the plasma membrane, and were not merely rolling on the surface of the cells.

Plane membrane strain calculated 66 msec into the loading correlated well with relative calcium changes ($r^2 = 0.75$) taken at the same time point (Fig. 9). Quasi-static, or low strain rate, experiments resulted in no significant calcium increase. There was no difference in deformation or calcium response for different gap distances (0.025 cm, average $d\epsilon/dt = 9.2$ sec^{-1}, $n = 5$ and 0.050 cm, average $d\epsilon/dt = 2.3$ sec^{-1}, $n = 3$), indicating that strain rates beyond 1 sec^{-1} unequivocally elicit a calcium influx (1.17 ± 0.05, relative change ± SEM), perhaps in a thresholding fashion.

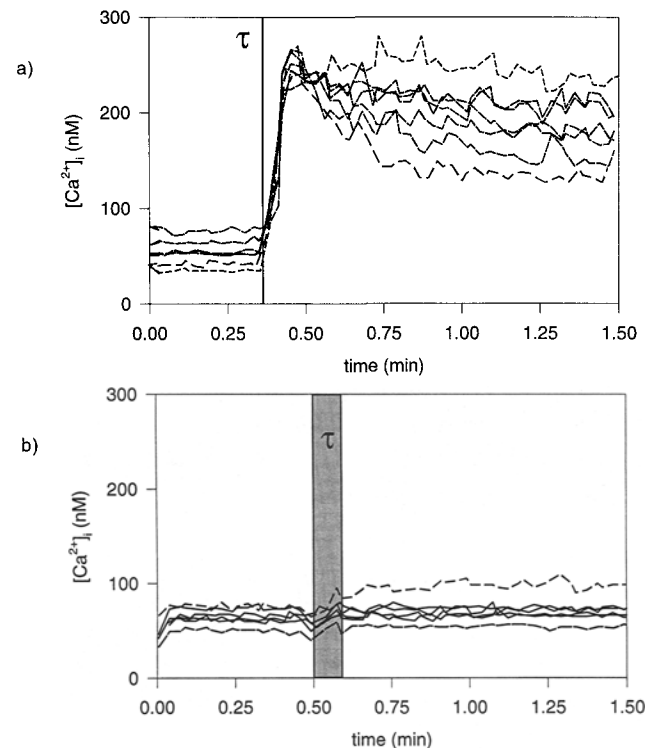[Ca^{2+}]$_i$ was found to increase within 1 sec of applica-

FIGURE 10. The rate dependence calcium response in neurons subjected to high rate and quasistatic shear stress, τ. Each trace represent an individual cell from a representative experiment. (a) Rapid fluid shear stress (pulse indicated by solid vertical line: $\tau = 20$ dyne/cm^2, rise time = 25 msec, pulse duration = 200 msec) causes an immediate rise in intracellular free calcium. (b) Quasistatically applied shear stress (indicated by gray box: $\tau = 20$ dyne/cm^2, rise time = 2 sec, duration = 4 sec) elicits little or no increase in intracellular free calcium.
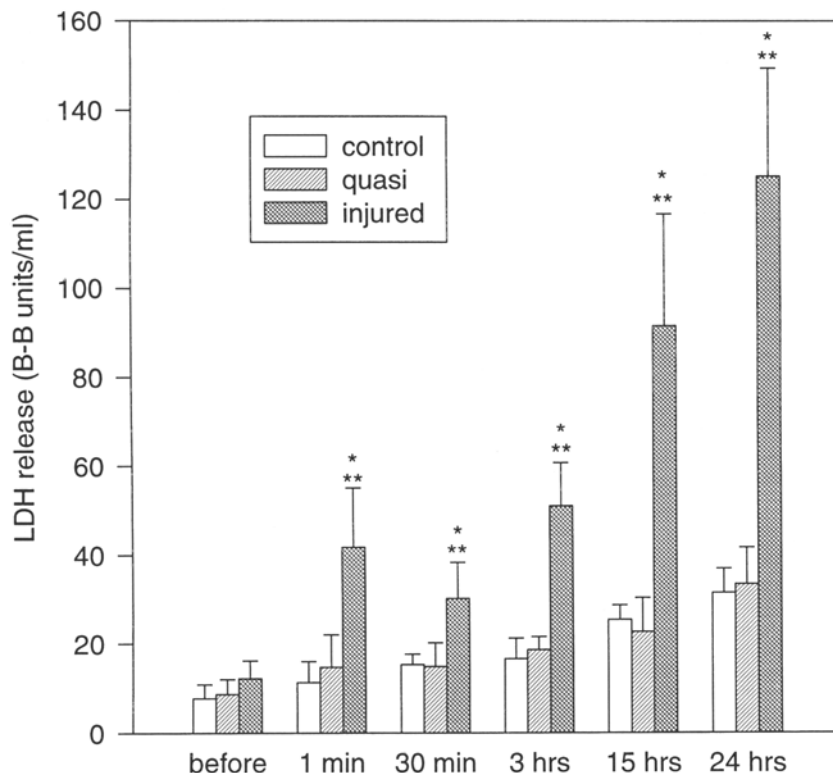
FIGURE 11. Time course of LDH release in injured neurons. Each bar represents the average of eight experiments. Error bars are the standard errors of the means. Control cells were loaded into the CSID but not injured; the hatched bars represent quasistatic experiments ($\tau = 20$ dyne/cm^2, rise time = 2 sec, duration = 4 sec); and the cross-hatched bars symbolize LDH values for high rate experiments ($\tau = 20$ dyne/cm^2, rise time = 25 msec, duration = 200 msec). *Significant from controls ($p < 0.02$); **significant from quasistatic controls ($p < 0.02$).

tion of fluid shear stress. Resting levels of $[Ca^{2+}]_i$ were 50 to 80 nM and rose significantly to levels of 200 to 500 nM in response to high strain rate loading conditions. Low strain rate loading conditions produced no significant calcium response (Fig. 10). These results indicate that cultured neurons have a threshold rate dependence to mechanical loading. LDH release from NT2-N cells subjected to high strain rate loading conditions at 24 hr was significantly higher than static and quasistatic conditions (Fig. 11). In addition, staining with Live/Dead stain 24 hr after the insult revealed an increasing number of dead cells from the center of the disk to the outer radial edge for high rate experiments (Fig. 12).

DISCUSSION

In vitro modeling of inertial injury in neurons provides an opportunity to control and simplify the complex loading environment that accompanies TBI, yielding information about cellular function that would otherwise be difficult to attain. In particular, the CSID allows controlled hydrodynamic stress to be applied, while measuring cellular response. This model isolated a component of traumatic injury, namely rapid deformation of neurons, which is characteristic of several clinically relevant forms of brain injury (9). The influence of systemic effects was eliminated, permitting greater control over the immediate environment. The simplified setting of a cell culture system allows greater control when introducing pharmaco-

logical agents and presents a basic framework on which multiple cell systems and *in vivo* experiments can be based.

The usefulness of a cell culture model relies on the appropriate design and implementation of the apparatus. Modeling acceleration injury on a cellular level requires an estimation of the relevant mechanical surroundings to best mimic the loading conditions that the cells experience. It is not merely enough to damage cells, because the deformation of the cells in unknown. Understanding the mechanical response is equally important as uncovering the functional outcome, because it is an initial mechanical event that triggers biochemical events. Ultimately, it is the mechanism by which the outcome measure occurs that is of interest and, therefore, it is critical that the loading be accurately characterized.

A force on the cells was generated by rapid fluid flow, an input that was readily quantified using basic fluid dynamics principles. Although the initial approximation of the shear stress from the azimuthal velocity was reasonable, visualization of the flow in the CSID indicated that a degree of radial velocity contributed to the total flow field for all configurations. Therefore, a finite element analysis was conducted to determine the influence of the radial component of velocity to the shear stress at the bottom disk. The magnitude of resultant shear stress calculated from both numerical and analytical means agreed very well. Smaller gap distances better approximated the assumption of infinite disks used in the first-order analytical

derivation, which is depicted in the dye experiment where the ratio of vectors in the r-direction to the resultant vector is much less for 0.025 cm than for 0.050 cm. The differences between the two solution schemes (Fig. 5) at small time points may be attributed to the elimination of v_r terms. For the smaller gap distance used, this difference was not detected, but in the $h = 0.050$ cm case, deviations in the start-up profile were evident. As expected, solution of the full Navier-Stokes equation was a better estimation of the start-up profile for the shear stress at the bottom disk of a parallel disk viscometer configuration, especially for h/r values >0.02. The azimuthal velocity solution scheme, rather, is better suited for estimations of steady-state problems.

Although the macroscopic flow patterns can be accurately described, the actual fluid shear stress on the cells is affected by spatial orientation and location of the cells on the cell plate and by cellular geometry. To relate mechanical input to cellular response, ideally the force on each cell should be known. Because of the difficulty in measuring individual cell forces, we assumed that the shear stress was uniform across a microscope field of cells and the same as for an equivalent plane wall. The shear stress distribution varied <2% for a field of 200 μm. Furthermore, the distribution of shear stress over the cells was considered when interpreting the strain data.

The mechanical response, namely cell surface strain, was measured by using fluorescent video analysis. This technique can be used in any device given that the substrate does not move during stimulation. Many investigators report the strain or displacement experienced by the substrate to which the cells are attached (2,5,32). Without knowing the complex dynamics of the cell-substrate attachments, it is an estimate to describe strain in this manner. In fact, Barbee et al. (1) found anisotropic strains between cell bodies and lamellipods in smooth muscle cells subjected to a uniform substrate strain. Using fluorescent microbeads, it is possible to obtain a more realistic approximation of strain and strain rate that a cell experiences under a given set of loading conditions.

The wide range of strains observed may be explained by the variation in local forces, and in the organization and morphology of the neurons studied. NT2-N cells exhibit polarity and usually have one axon and many dendrites projected from a hemispherical cell body when in a two-dimensional culture. The physical interaction between cells (i.e., whether cells are in clumps or are by themselves) may alter the force a cell actually experiences. The surface area exposed to flow forces is greater in single cells than for individual cells within a clump. The actual force on a hemispherical mound on an infinite wall was calculated to be 4 times greater than that for a plane wall, even if the dimensions of the protrusion (cell) are much less than the dimensions of the chamber (gap distance) (13). This analysis by Hyman(13) also identified a distri-
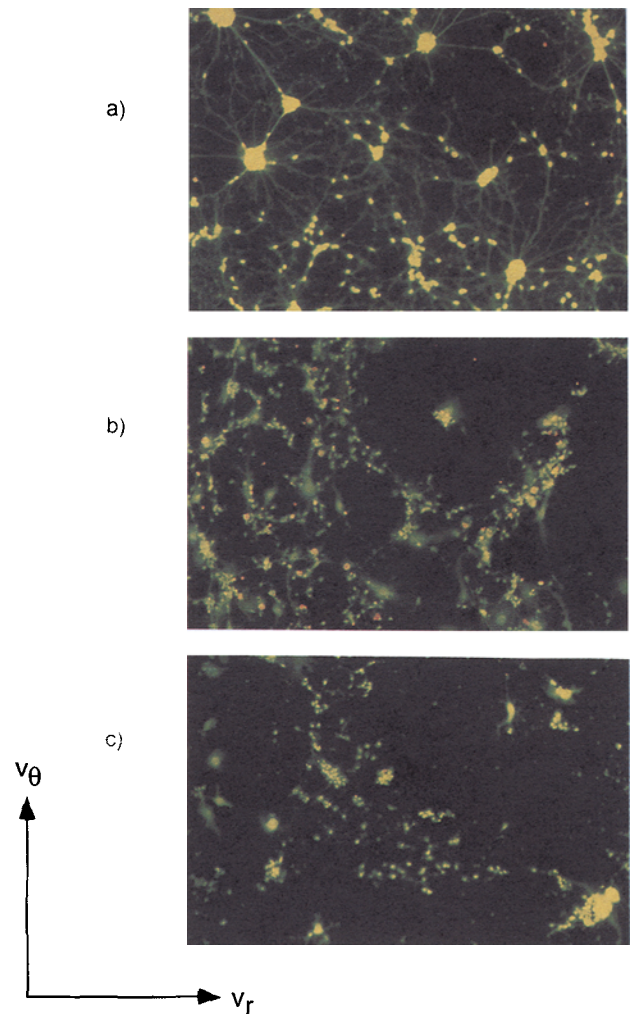

FIGURE 12. Live/Dead stain in injured neurons at 24 hr. Calcein-loaded cells appear green; the dye is trapped in viable cells, because an active cytosolic esterase must cleave the acetoxymethyl ester off the fluorescent probe to be seen. Dead cells appear as small red dots, which are ethidium homodimer-loaded nuclei. This DNA stain can only cross the membranes of dead cells. Cells were observed using a filter set with an excitation range of 450–490 nm; dichroic, 510 nm; emission, 520 nm; and a Nikon 10x fluorescent objective. Geometric axes for velocity directions are shown. (a) Cells at the center of a disk where $\tau = 0$; (b) cells at the radius used for calcium measurements ($r = 1.0$ cm) on the same disk, $\tau = 20$ dyne/cm^2; and (c) cells at the outer edge ($r = 2.5$ cm) of the same disk, $\tau = 50$ dyne/cm^2.

bution of normal forces over the mound that are dependent on the local flow field, which would combine with the tangential forces to determine the deformation of the mound. Neurons are rather spherical in shape and these considerations readily apply. This may also explain why neurites experience less strain than cell bodies, whether they appear in singles or in clumps. There may also be differences in regional adhesion properties within a cell that may account for differences in mechanical behavior.

The orientation of the cells may also influence the me-

chanical response. For instance, if the processes of a cell were aligned in the θ-direction, it may experience more stress than a cell aligned in the r-direction, due to a greater $\tau_{z\theta}$. Similarly, if a cell body were imbedded in an aggregate of cells, it may be protected, both from a mechanical standpoint (the force would be distributed such that each cell would be exposed to only a fraction of the total force) and from a chemical standpoint (diffusion of extracellular substances would be limited due to reduced surface area, and uptake of expelled intracellular milieu would be shared by more cells, reducing the amount of buffering responsibility per cell). In fact, single cells had higher strains, higher peak calcium values, and were more likely to die than cells in clumps of four or more cells as measured by the Live/Dead stain.

The strain measured in this system is the plane strain on the top portion of the cell in the $r\theta$-plane. Other strains (*i.e.*, strains in the zr- and $z\theta$-planes) may play a role in the response and, although they were not measured here, warrant consideration. The strain rates given here may also be underestimated. The strain produced in the cells must slightly lag the onset of stress due to the intrinsic viscoelastic properties, yet the earliest time point available for analysis was 66 msec, at least twice as long as the time for the shear stress to reach a maximum value.

The extent of cellular damage that occurs is hypothesized to be a function of the deformation and rate of deformation. Due to the viscoelastic nature of cells, the resulting force in cells deformed at a low rate (<1 sec^{-1}) is lower than for high rate (>1 sec^{-1}) conditions, leading to different mechanical behavior. In addition, high strain rates do not allow the cell constituents time to rearrange and adjust to the stress; therefore, even a small deformation may be enough for physical disruption of the cell. Rate-dependent cell damage is hypothesized to arise as transient membrane pores (29), through which free calcium enters and LDH effluxes. $[Ca^{2+}]_i$ increases measured within the first 100 msec of loading corresponded with cellular strain, indicating that a change in membrane properties may be linked to the deformation response of the neurons to hydrodynamic shear forces. Furthermore, simultaneous measurement of strain and $[Ca^{2+}]_i$indicated that strains in cells subjected to the same level of stress varied, as did the calcium response, implicating strain as an instigator of cellular response. It is important to correlate the strain and strain rate with the extent of damage in this manner to develop tolerance criteria at the cellular level.

High strain and strain rates may increase the membrane permeability. A stretch-induced increase in membrane conductance to several ions, including calcium, has been observed in several tissue and cellular systems (2,7,8,14,23,33). Calcium influx may be caused by an increase in membrane permeability due to high strains and

strain rates. We have shown that high strain levels can be generated and that $[Ca^{2+}]_i$ changes are dependent on the strain rate.

Not only does $[Ca^{2+}]_i$ increase, but in cultures with this acute response cell damage and death were evident at 24 hr, implicating high levels of cytosolic calcium in the injury cascade. When extracellular calcium was removed from the bathing buffer, the acute calcium response was reduced and the cells protected from damage at 24 hr, indicating that, although the calcium signaling cascade may be complex after mechanical loading, the continued influx of calcium is necessary for cell death in this model (data not shown). The immediate (1-min postinjury) release of LDH, regardless of extracellular buffer composition, suggests that a mechanical breakdown of the cell membrane is a prominent part of the acute response, because a chemical insult gradually causes a loss in membrane integrity over 24 hr. Live/Dead staining at 24 hr confirms that the neurons are dying and that the rate of loading, and therefore the rate of deformation, is important in the response of NT2-N cells to shearing injury. The detachment of cells at the outer radial edge could be due to the high rates of loading combined with high levels of shear stress or to subsequent cell death and detachment. Because early time points revealed a low number of cells at the periphery of the disk, the former is a more likely explanation. The radius at which calcium measurements were taken ($r = 1.0$ cm) was exempt from this loss of cells, however. Viewing the neurons using Live/Dead staining qualitatively illustrated the cell death resulting from shear-induced deformations.

The injury model described here has a wide range of applications within cellular biomechanics. The importance of loading rate is apparent and should be considered when describing the effects of mechanical loading of cultured cells. Within the trauma field, the variable and reproducible mechanical input to the cells is critical when comparing injury patterns to control conditions. The deformation and functional responses to various levels and rates of mechanical inputs can then be confidently measured. A single cell type or a multicell system can be used and the extracellular environment can be easily manipulated and sampled, rendering it a powerful technique for studying mechanical injury *in vitro*. The CSID is capable of real-time monitoring; cells are visible throughout the experiment, because the substrate to which they are attached does not deflect or deform. The clear light path also permits observation and measurement before, during, and after the injury in fluorescent and incandescent light, widening the ability to measure any physiological parameter for which tools exist. Once a pattern can be established, various mechanisms can be investigated by adding appropriate agonists and antagonists. Additional chemical insults can be superimposed onto the mechanical trauma as

well, yielding new insight into the response of cells to simulated injury.

REFERENCES

1. Barbee, K. A., E. J. Macarak, and L. E. Thibault. Strain measurements in cultured vascular smooth muscle cells subjected to mechanical deformation. *Ann. Biomed. Eng.* 22:14–22, 1994.
2. Cargill, R. S., and L. E. Thibault. Acute alterations in $[Ca^{2+}]_i$ in NG108-15 cells subjected to high strain rate deformation and chemical hypoxia: an *in vitro* model for neural trauma. *J. Neurotrauma* 13:395–407, 1996.
3. Davies, P. F., F. Dewy, S. R. Bussolari, E. J. Gordon, and M. A. Gimbrone. Influence of hemodynamic forces on vascular endothelial function. *J. Clin. Invest* 73:1121–1129, 1984.
4. Dewey, C. F. J., and S. R. Bussolari. The dynamic response of vascular endothelial cells to fluid shear stress. *J. Biomech. Eng.* 103:177–185, 1981.
5. Ellis, E. F., J. S. McKinney, K. A. Willoughby, S. Liang, and J. T. Polishock. A new model for rapid stretch-induced injury of cells in culture: characterization of the model using astrocytes. *J. Neurotrauma* 12:325–339, 1995.
6. Evans, E., and B. Kukan. Passive mechanical behavior of granulocytes based on large deformation and recovery after deformation tests. *Blood* 64:1028–1035, 1984.
7. Galbraith, J., and L. E. Thibault. Mechanically induced depolarizations in the squid giant axon. *J. Biomech. Eng.* 115:13–22, 1993.
8. Ganot, G., B. Wong, L. Binstock, and G. Eherenstein. Reversal potentials corresponding to mechanical stimulation and leakage current in Myxicola giant axons. *Biochim. Biophys. Acta* 649:487–491, 1981.
9. Gennarelli, T. A. Mechanisms of brain injury. *J. Emerg. Med.* 11:5–11, 1993.
10. Gennarelli, T. A., and L. E. Thibault. Biological models of head injury. In: Central nervous system trauma status report, edited by J. T. Povlishock. Bethesda, MD: NINCDS, NIH, Public Health Services, 1984.
11. Graham, D. I., J. H. Adams, D. Doyle, I. Ford, T. A. Gennarelli, A. E. Lawrence, W. L. Maxwell, and D. R. McLellan. Quantification of primary and secondary lesions in severe head injury. *Acta Neurochir.* 57:41–48, 1993.
12. Guilak, F. Volume and surface area measurement of viable chondrocytes *in situ* using geometric modelling of serial confocal sections. *J. Microsc.* 173:245–256, 1994.
13. Hyman, W. A. Shear flow over a protrusion from a plane wall. *J. Biomech.* 5:45–48, 1972.
14. Landsman, A. S., D. F. Meaney, R. S. Cargill, E. J. Macarak, and L. E. Thibault. 1995 William J. Stickel Gold Award. High strain rate tissue deformation: a theory on the mechanical etiology of diabetic foot ulcerations. *J. Am. Podiatr. Med. Assoc.* 85:519–527, 1995.
15. Leal, G. L. Laminar Flow and Convective Processes: Scaling Principles and Asymptotic Analysis. Boston: Butterworth-Heinemann, 1992.
16. Levich, V. G. Physicochemical Hydrodynamics. Englewood Cliffs, NJ: Prentice-Hall, Inc., 1962.

17. Lucas, J. H., and A. Wolf. *In vitro* studies of multiple impact injury to mammalian CNS neurons: prevention of perikaryal damage and death by ketamine. *Brain Res.* 543:181–193, 1991.
18. Margulies, S. S., L. E. Thibault, and T. A. Gennarelli. Physical model simulations of brain injury in the primate. *J. Biomech.* 23:823–836, 1990.
19. Nomura, H., C. Ishikawa, T. Komatsuda, J. Ando, and A. Kamiya. A disk-type apparatus for applying fluid shear stress on cultured endothelial cells. *Biorheology* 25:461–470, 1988.
20. Orrenius, S., D. J. McConkey, G. Bellomo, and P. Nicotera. Role of Ca^{2+} in toxic cell killing. *Trends Pharmacol. Sci.* 10:281–285, 1989.
21. Pleasure, S. J., C. Page, and V. M. Y. Lee. Pure, postmitotic, polarized human neurons derived from NTera 2 cells provide a system for expressing exogenous proteins in terminally differentiated neurons. *J. Neurosci.* 12:1802–1815, 1992.
22. Rand, R. P., and A. C. Burton. Mechanical properties of the red cell membrane. *Biophys. J.* 4:115–135, 1964.
23. Saatman, K. E., and L. E. Thibault. Axonal injury studied in a single myelinated nerve fiber model. *J. Neurotrauma* 11:125, 1994.
24. Sato, M., D. P. Theret, L. T. Wheeler, N. Ohshima, and R. M. Nerem. Application of the micropipette technique to the measurement of cultured porcine aortic endothelial cell viscoelastic properties. *J. Biomech. Eng.* 112:263–268, 1990.
25. Schanne, F. A. X., A. B. Kane, E. E. Young, and J. L. Farber. Calcium dependence of toxic cell death: a final common pathway. *Science* 206:700–702, 1979.
26. Shepard, S. R., J. B. G. Ghajar, R. Giannuzzi, S. Kupferman, and R. J. Hariri. Fluid percussion barotrauma chamber: a new *in vitro* model for traumatic brain injury. *J. Surg. Res.* 51:417–424, 1991.
27. Siesjo, B. K. Basic mechanisms of traumatic brain damage. *Ann. Emerg. Med.* 22:959–969, 1993.
28. Simon, S. I., and G. W. Schmid-Schonbein. Cytoplasmic strains and strain rates in motile polymorphonuclear leukocytes. *Biophys. J.* 58:319–332, 1990.
29. Thibault, L. E. Isolated tissue and cellular biomechanics. In: Accidental injury: biomechanics and prevention, edited by R. P. Nahum and J. W. Melvin. New York: Springer-Verlag & Co., 1993, pp. 512–537.
30. Trump, B. F., and I. K. Berezesky. The role of cytosolic Ca^{2+} in cell injury, necrosis and apoptosis. *Curr. Opin. Cell Biol.* 4:227–232, 1992.
31. Watson, P. A. Function follows form: generation of intracellular signals by cell deformation. *FASEB J.* 5:2013–2019, 1991.
32. Winston, F. L., E. J. Macarak, S. F. Gorfien, and L. E. Thibault. A system to reproduce and quantify the biomechanical environment of the cell. *J. Appl. Physiol.* 67:397–405, 1989.
33. Zimmermann, U., G. Pilwat, A. Pequeux, and R. Gilles. Electro-mechanical properties of human erthyrocyte membranes: The pressure-dependence of potassium permeability. *J. Mem. Biol.* 54:103–113, 1980.